Scripta Materialia 193 (2021) 81–85

Contents lists available at ScienceDirect

Scripta Materialia

journal homepage: www.elsevier.com/locate/scriptamat

Ensuring the strength and ductility synergy in an austenitic stainless steel: single- or multi-phase hetero-structures design

Yong Li[a,b], Wei Li[a,b,*], Shilei Li[c], Na Min[d], Laizhu Jiang[e], Qinglong Zhou[e], Xuejun Jin[a,b]

[a] Shanghai Key Laboratory of Material Laser Processing and Modification, Shanghai Jiao Tong University, Shanghai 200240, PR China
[b] Institute of Advanced Steels and Materials, School of Materials Science and Engineering, Shanghai Jiao Tong University, Shanghai 200240, China
[c] Beijing Advanced Innovation Center for Materials Genome Engineering, State Key Laboratory for Advanced Metals and Materials, University of Science and Technology Beijing, Beijing 100083, China
[d] Key Laboratory for Microstructures, Shanghai University, Shanghai 200444, China
[e] Research Institute of Tsingtuo Group Co.,Ltd., Fuan 355006,China

ARTICLE INFO

Article history:
Received 4 September 2020
Revised 20 October 2020
Accepted 22 October 2020

Keywords:
Heterogeneous microstructure
Transformation-induced plasticity
Twinning-induced plasticity
Dislocation

ABSTRACT

Heterogeneous microstructures have been proposed to optimize the mechanical properties in the respect of strength and ductility synergy in many alloy systems. In this work, the multi-phase hetero-structured microstructure consisting of fine grains and coarse grains where the ferrite is embedded in the vicinity of the nano-grains was obtained by regulating the thermomechanical processing parameters. A yield strength of 1.2 GPa which is more than two times higher than the coarse grained counterpart with less uniform elongation loss is achieved in the multi-phase hetero-structured steel. The microscopic load transfer in this complex microstructure is investigated by the in situ high energy synchrotron X-ray diffraction. The persistent strain hardening is ascribed to the hetero-deformation induced stress associated with the joint activation of transformation-induced plasticity (TRIP) and twinning-induced plasticity (TWIP) effects. As a comparison, the single-phase hetero-structured steel exhibits little lower strength but higher uniform ductility.

Transformation-induced plasticity (TRIP) is an effective approach to improve the work hardening capacity to cope up with the increase in flow stress and retain ductility, which has been documented in the TRIP steels [1], quenching and partitioning (Q&P) steels [2] and medium manganese steels [3]. Some austenitic steels with low stacking fault energy (SFE) benefiting from the TRIP-assisted delayed catastrophic failure are inclined to leap out of the conventional trade-off between the strength and ductility [4,5]. However, the strain localization and unstable necking could be also initiated due to the deformation incompatibility in the multi-phase matrix when the grain size, volume fraction, phase distribution and hardness of the constituent phases are not optimized [6,7].

An attractive strengthening pathway to alleviate the inverse strength-ductility dilemma in the austenitic steels, viz., introducing the gradation of grain size into materials is becoming a charming topic in recent years [8-10]. The development of the hetero-structured alloys aroused an ongoing interest for ensuring the uniform elongation (UEL) at high and even ultrahigh strength by triggering the intrinsic hetero-deformation induced (HDI) hardening owing to the interfacial storage of the geometrically necessary dislocations (GNDs) [11]. Such materials acquired through massive plastic deformation and subsequently partial recrystallization generally possess hierarchical grain size covering from nano-grains (NGs) and ultrafine grains (UFGs) to coarse grains (CGs) [8,10]. However, the knowledge on how to achieve the balance between the hard domains (NGs and UFGs) and ductile domains (CGs) in terms of the polarity of strength and ductility combination in the hetero-structured metallic materials with gratifying mechanical response still remains elusive [12], viz., the NGs exhibit high yield strength but low capacity of dislocation storage without contributing to global work hardening of the bulk materials [13]. Therefore, extra strain hardening mechanisms such as TRIP and twinning-induced plasticity (TWIP) effects to sustain uniform deformability are urgently expected for the steels yielding at the magnitude of gigapascal.

The austenitic stainless steel studied in this work is composed of (by weight) 0.07% C-0.42% Si-6.15% Mn-18.14% Cr-3.03% Ni-0.11% Mo-1.62% Cu-0.23% N and balanced Fe. The steel was melted in a vacuum and cast into round billets. After homogenization, the billets were subjected to hot-rolling with the final thickness of 6.3

* Corresponding author: Tel.:+86-21-54745420.
E-mail address: weilee@sjtu.edu.cn (W. Li).

https://doi.org/10.1016/j.scriptamat.2020.10.041
1359-6462/

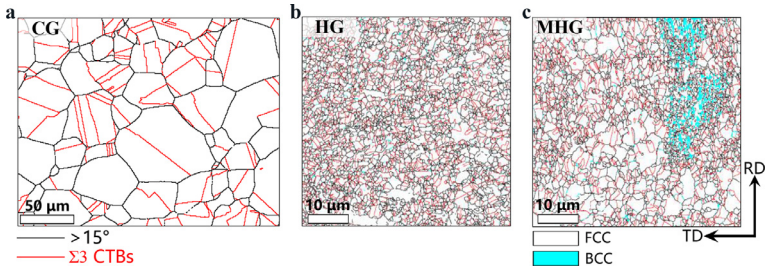

Fig. 1. Typical EBSD IQ maps overlaid by various GBs of the as-received CG steel (a), HG steel (b) and MHG steel (c).

mm, followed by water quenching to room temperature. The as-received microstructure (CG steel) is fully austenite with an average grain size of ~21 μm after solution treatment. Prior rolling deformations were conducted using unidirectional rolling at cryogenic temperature (CT, 77 K) and room temperature (RT, 298 K). The as-received material was initially rolled at CT to the thickness of 5.2 mm by five passes. Thereafter, the plate was further subjected to cold rolling at RT, finished with the final thickness of 1.1 mm. For the single-phase sample, the sheets were subjected to recrystallization annealing at 700 °C for 15 min. For the multi-phase one, the sheets were initially subjected to tempering at 400 °C for 1h and subsequently annealing at 700 °C for 15 min.

The in situ SXRD measurement was carried out on the 11-ID-C beam line of the Advanced Photon Source, Argonne National Laboratory, USA. The X-ray beam with an energy of ~105 keV (λ=0.11742 Å) was used to detect the microstructural evolution and lattice strain in real time. The lattice stress were calculated using $E^{hkl}(d^{hkl}-d_0^{hkl})/d_0^{hkl}$, where $E^{hkl}$is the diffraction elastic constant, $d_0^{hkl}$and $d^{hkl}$are the d-spacing of the (hkl) lattice plane at zero applied stress and instantaneously applied stress, respectively. The austenite volume fractions (V_γ) were estimated by the following equation: $V_\gamma=\frac{1.4I_\gamma}{I_\alpha+1.4I_\gamma}=\frac{\frac{1.4}{n}\sum_{i=1}^{n}I_{\gamma,i}^{hkl}}{\frac{1.4}{n}\sum_{i=1}^{n}I_{\gamma,i}^{hkl}+\frac{1}{m}\sum_{i=1}^{m}I_{\alpha,i}^{hkl}}$, where the $I_{\gamma,\alpha}$is the integral intensity of specific diffraction peaks. Microstructural investigations were performed on RD-TD sections (RD-rolling direction, TD-transverse direction). The specific experimental procedures of typical microstructural analysis and quasi-static uniaxial tensile tests can referred to our previous study [14].

Fig. 1 shows the image quality (IQ) pattern overlaid by various grain boundaries (GBs) of the CG, HG (hierarchical grain) and MHG (multi-phase hierarchical grain) steels. Σ3 coherent annealing twins (CTBs) were all detected in these samples. In contrast to the single-phase microstructure in Fig. 1b, Fig. 1c indicates that the dual-phase regions are randomly distributed in the austenitic matrix along the RD in the MHG steel. The hierarchical grains of the partially recrystallized austenitic matrix in the HG steel were divided into coarse grains (CGs, > 1μm, fully recrystallized regions) with mean diameter of 1.47 μm and fine grains (FGs, ≤ 1μm, partially recrystallized regions) with mean diameter of 343 nm. As to the MHG steel, the CGs with mean diameter of 1.60 μm and the FGs with mean diameter of 235 nm were revealed in the austenitic matrix. Meanwhile, a few austenite grains with average size below 100 nm are mainly embedded in the vicinity of the ferrite. According to the XRD results in Fig. S1, the volume fractions of bcc phase were estimated as 17.1 vol%, 4.7 vol% and 14.3 vol% in the as-rolled, HG and MHG sample, respectively.

The engineering stress-strain (σ-ε) curves of these steels are shown in Fig. 2a. In general, the initial drop and a subsequently rapid increase of the work hardening rate (Θ) are known to usually occur in the multi-phase alloys with varying yield stresses [7,15-18]. An upper yield strength of ~1.2 GPa was obtained for the hetero-structured steels, such high strength is 2~3 times that of the CG counterpart, with little loss in ductility. The corresponding true σ-ε and Θ curves are plotted in Fig. 2b. It is worth noting that the Θ of the CG steel plunged straight to the onset of the local necking, while the two hetero-structured steels exhibit an up-turn at 0.05 true strain. Akin to the high strength steels, the plastic instability is ascribed to the occurrence of Lüder strains [3]. Apart from the mobile dislocations in the ferrite, the high density interface could also promote the rapid increase of mobile dislocations, contributing to the discontinuous yielding [19,20]. Besides, the elevated Θ value at ε=0.21 was revealed in the HG steel.

The in situ X-ray and ex-situ EBSD measurements were performed for the MHG steel. Fig. 3a reveals the evolution of martensite volume fraction during deformation, and the transit region implied the avalanche of martensitic transformation (~25 vol%). In Fig. 3b, the lattice stress of $\{211\}_{BCC}$ and $\{311\}_{FCC}$ grain families were chosen for in-depth analysis since their insensitivity to intergranular strain [21]. By evaluating the stress imposed on the $\{211\}_{BCC}$, the critical stress for the martensite to appear is about 1750 MPa. At this stress value, the activation of local necking can be detected from the lattice stress of $\{311\}_{FCC}$ grain families. With proceeding plastic deformation, further increase of macroscopic stress gives rise to a spontaneous and massive transformation on the global scale, eventually resulting in the catastrophic failure of the sample. As to the ex-situ EBSD characterization shown in Fig. 3c, the initial microstructure was divided into CG region in the upper portion and FG region in the lower portion. The partial martensitic transformation was obviously detected in some individual CGs.

As to the deformation substructures, the Kernel average misorientation (KAM) map of the CG steel at 0.1 true strain in Fig. S2a shows large local misorientation up to 3.6 and unconspicuous martensitic transformation behavior around the high-angle grain boundaries (HAGBs). The profuse LAGBs illustrated in Fig. S2b substantiates the severe deformation near the HAGBs [22], implying the dominance of dislocation-mediated plasticity in the early deformation stage of the CG steel. With proceeding deformation stage, apart from the duple twinning systems that were demonstrated by the selected area diffraction (SAED) pattern (Fig. S2c and d), the interrupted 0.4 strained CG steel (fractured sample) exhibited plenty of dislocation tangles/cells near the TBs (Fig. S2d). Fig. 4a~f show the TEM images of interrupted 0.1 and 0.2 strained MHG steel. Only a few stacking faults (SFs) and deformation twins (DTs) were found in the FGs, the major proportion of the FGs including the finer NGs interior exhibited no apparent dislocation accumulation in the grain interior (Fig. 4a). Owing to the high initial dislocation density in the FGs formed through partial recrystallization, the dynamic recovery associated with the spreading of trapped lattice dislocations into GBs led to no significant dislocation storage inside the grains [23]. In contrast, the single twinning system and martensitic transformation appeared in the CGs. In Fig. 4b, the deformation twinning having a {111} <11> crystallographic component were demonstrated by the SAED pattern in the inset graph. The matrix near to the newly formed lath shaped martensite was filled with dislocation tangles and cells (Fig. 4c),

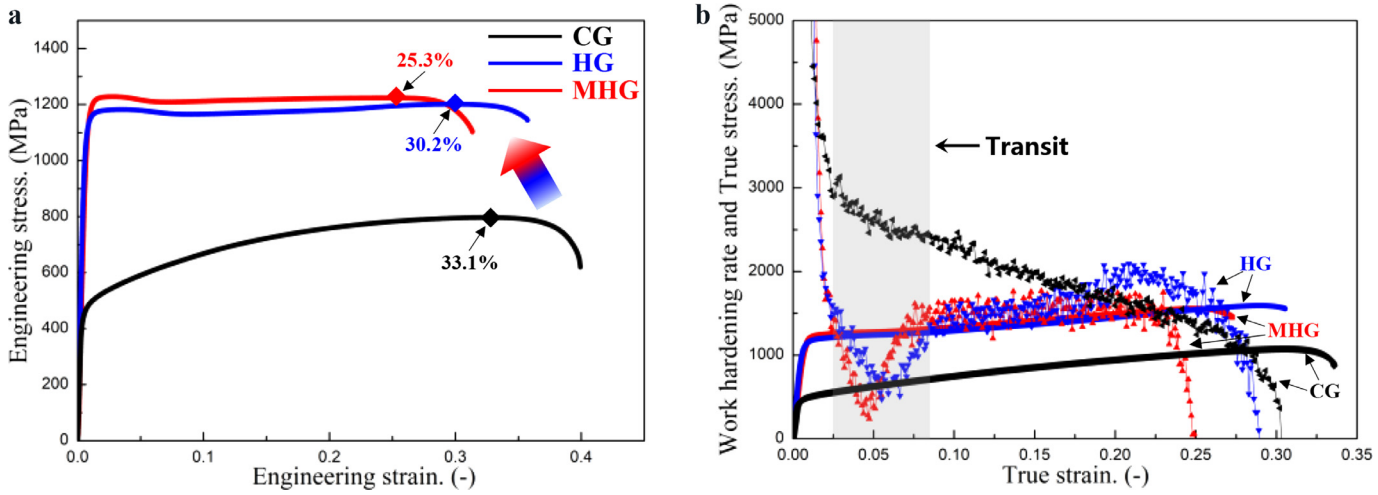

Fig. 2. The engineering σ-ε (a) and corresponding Θ (b) curves of the CG and hetero-structured steels.

which derived from the onset of plastic deformation in response to the adjacent martensitic transformation. With proceeding plastic deformation up to 0.2, the duple twinning systems were revealed in the CGs (see Fig. 4f). Likewise, the martensitic transformation was identified by the SAED in Fig. 4e. The martensite exhibited coherent orientation relationship with the austenitic matrix, viz., $[110]_{\gamma}$ // $[111]_{\alpha'}$ and $(\bar{1}\bar{1}1)_{\gamma}$// $(0\bar{1}1)_{\alpha'}$, and the untransformed austenite was revealed by high density dislocations (Fig. 4d). The appearance of the underlying deformation substructures in the MHG steel is ascribed to the trans-scale grain hierarchy. It is recognized that deformation twinning is restricted by grain refinement considering the higher critical stress for twinning in the finer grains [10,24], and the martensitic transformation can be suppressed in the finer grains thanks to the high elastic strain energy [19]. Therefore, only a few SFs and DTs were observed in the FGs (Fig. 4a and f). However, in the CGs, the increased resolved shear stress of another twinning system triggers the secondary twinning system since the primary twinning could change the crystallographic orientation [25]. Moreover, the intersecting twinning systems provided effective obstacles for the entanglement of dislocations from different slip systems and subsequently continuous strain hardening [26]. On the other hand, the nanoscale DTs and partial martensitic transformation progressively subdivided the original CGs into lamellar nancrystallites of ~200 nm, thus activating the dynamic Hall-Petch effect [8]. As to the HG steel, the interrupted 10% strained HG steel shown in Fig. S3 revealed that the partial martensitic transformation and deformation twinning both appeared in the CGs. Regarding the difference in deformation mechanisms among these two steels, nucleation of twins in the FGs were indicated in the HG steel while the FGs in the MHG steel almost exhibited defect-free morphology. Considering the thermomechanical processing parameters, the tempering

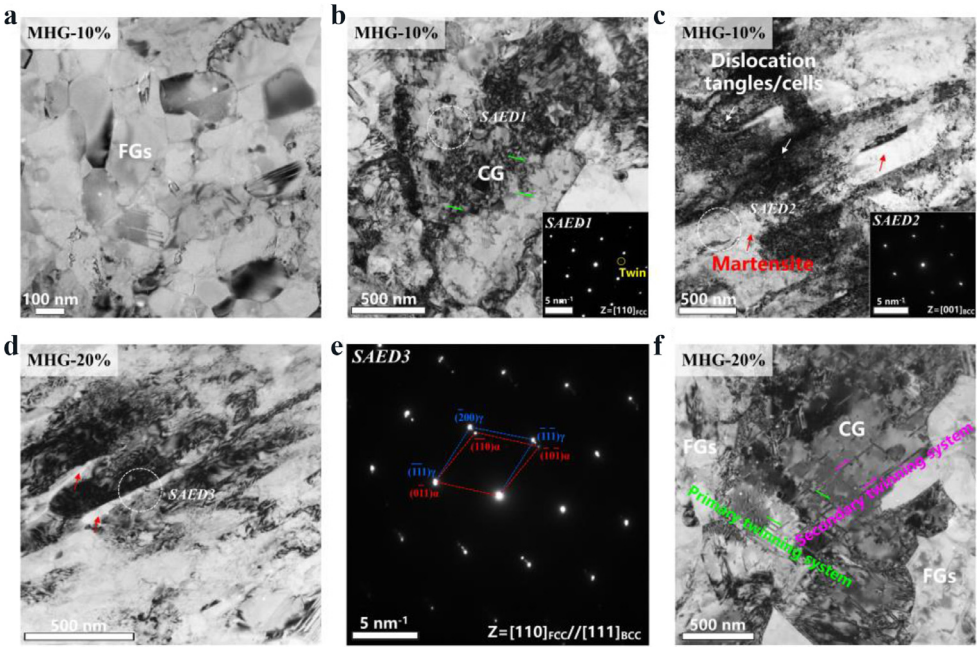

Fig. 4. The bright field images and corresponding SAED patterns of the interrupted strained MHG steel. In 10% strained specimens, (a) a few SFs and DTs are observed in the FGs, deformation twins (b) and partial martensite transformation (c) in the CGs are demonstrated by the inset SAED pattern, respectively. When the deformation proceeds to 20%, partial martensite transformation (d) and the coherent orientation relationship among the austenitic matrix and newly formed martensite are revealed by the SAED pattern (e), and duple twinning systems are indicated in the CGs, while the FGs almost exhibit defect-free morphology (f).

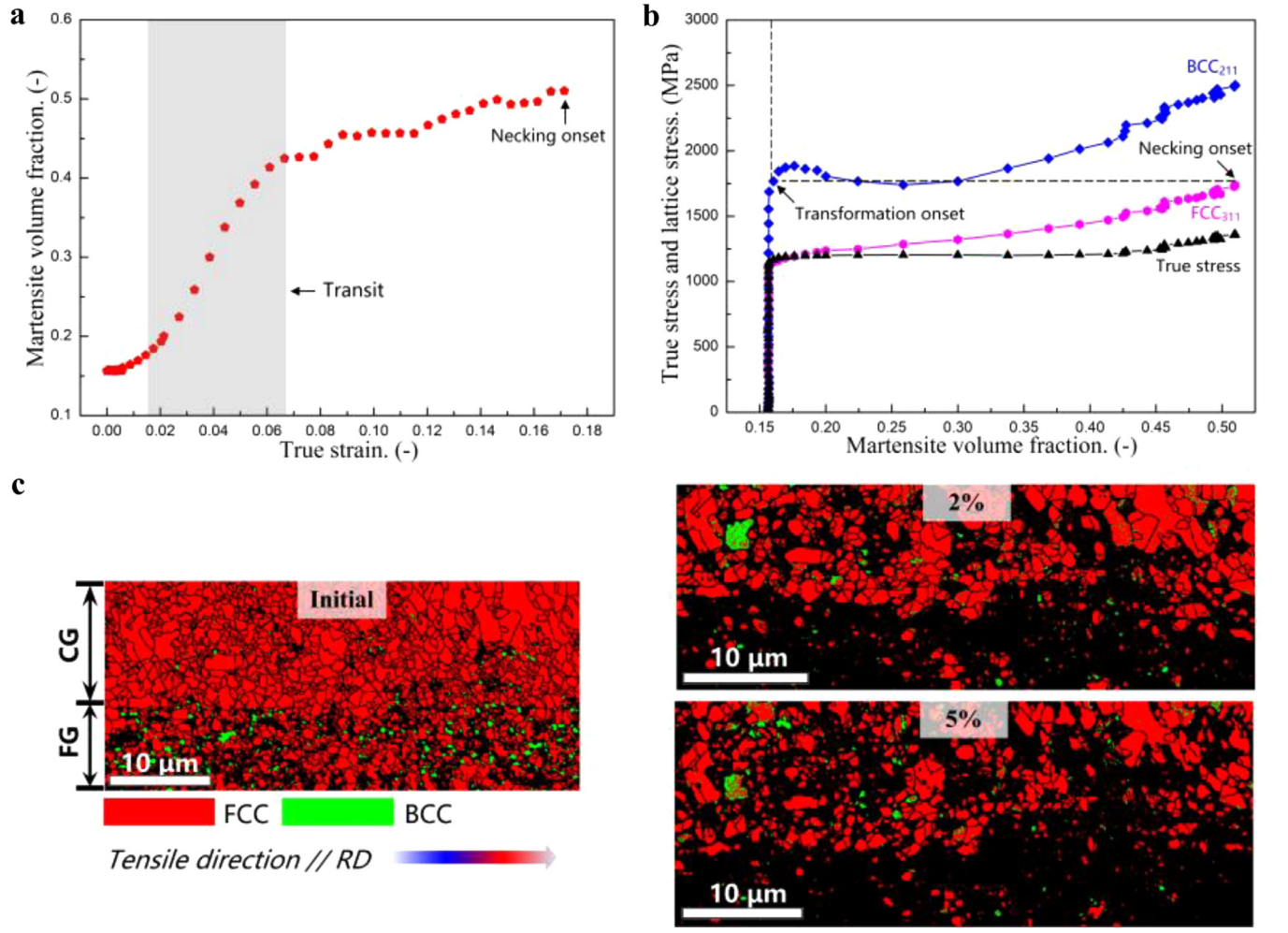

Fig. 3. In situ SXRD and ex-situ EBSD measurements of the MHG steel. (a) Evolution of the martensite volume fraction. (b) Lattice stress of austenite {311} and martensite {211} as a function of the martensite volume fraction. (c) Phase maps during ex-situ EBSD measurement where the red and green area account for the austenite and martensite, respectively.

treatment resulted in inhibited austenite reversion and heterogeneous recrystallization behavior in the MHG steel. Thus, smaller grain size of FGs and higher volume fraction of hard domains were obtained in the MHG steel, in which the CGs determined the uniform deformation. In contrast, the larger grain size of FGs in the HG steel promoted deformation twinning, thereby played similar role controlling the ductility. Furthermore, the concurrently activated deformation twinning in the FGs and CGs contributed to the global deformation compatibility, thus alleviated the plastic instability and delayed the martensitic transformation.

Regarding the work hardening behavior, the driving force that governs the nucleation of martensite under which stress- and strain- induced transformation occur can be expressed as following equation [27]:

$$\Delta G^{\gamma\to\alpha} = \underbrace{\Delta G_{ch}^{\gamma\to\alpha}}_{\text{I}} - \underbrace{\Delta G_{mech}}_{\text{II}} - \underbrace{\Delta G_{disl}}_{\text{III}} \quad (1)$$

where $\Delta G^{\gamma\to\alpha}$ is the total driving force of the system. Term I represents the chemical driving force, term II accounts for the mechanical driving force introduced by the compressive stress, and term III is the driving force required for the interface to overcome the dislocation density introduced during plastic deformation. The extremely high lattice stress (Fig. 3b) required for triggering martensitic transformation could suppress the TRIP effect in the CG steel. As expected, the XRD spectrums (Fig. S4) of the interrupted deformed samples of CG steel even at the fracture state hardly imply martensitic transformation. Consequently, the simple deformation mechanism and gradually saturated defects without martensitic transformation resulted in the continuous degradation of the strain hardening capability (Fig. 2b). For the MHG steel, the HDI stress originated from the multi-scale grain size and the interplay among hard domains (martensite and nano-precipitates) and soft one (fcc-based matrix), where the CGs were most susceptible to plastic deformation. On the one hand, the high density of interfaces serving as dislocation sources in the multi-scale matrix promoted the emission of dislocations, which is associated with the plastic strain partitioning. Furthermore, the macroscopic strain gradient enabled the formation of multiaxial stresses due to deformation incompatibility upon uniaxial tensile deformation [8], thus promoted the accumulation and interaction of dislocations particularly in the CGs interior. Consequently, higher driving force for martensitic transformation was generated within CGs. The newly created phase boundaries after martensitic transformation could provide fresh obstacles for dislocation motion and sustain the persistent strain hardening. Moreover, the deformation incompatibility associated with the grain size evolution involving the partial martensitic transformation and deformation twinning promoted the interfacial storage of the GNDs that were created by the plastic strain gradients near the GBs, phase boundaries and TBs in austenite as well, thereby improving the HDI stress and global strain hardening [28]. Addition-

ally, the plastic instability during initial deformation stage could also facilitate the avalanche of martensitic transformation by improving the dislocation density in the untransformed matrix owing to deformation incompatibility. In contrast, the relatively homogeneous matrix in the single-phase HG steel without ferrite postponed the TRIP effect into higher strain range, which was demonstrated by the XRD results (Fig. S5) of the 10% strained and fractured samples, i.e., the formation of 18.5 vol% and 44.1 vol% fresh martensitic, respectively.

In conclusion, the persistent strain hardening capacity of the MHG steel mainly originated from the jointly activated TRIP and TWIP effects over the entire uniform strain range. Single twinning system and martensitic transformation were nucleated in the CGs in the early deformation stage (ε=0.1) of MHG steel. The duple twinning systems were observed with progressive deformation up to ε=0.2. In contrast, the as-received CG steel was dominated with deformation twinning that was decorated by high density dislocation arrays with unconscious martensitic transformation behavior. As to the HG steel in the early deformation stage (ε=0.1), the CGs revealed partial martensitic transformation and deformation twinning behaviors, while the FGs exhibited deformation twinning as well. The avalanche of martensitic transformation during initial deformation stage occurred in the MHG steel, while the TRIP effect was postponed into larger strain range in the single-phase HG steel. In brief, higher strength was achieved by introducing hard domains into hetero-structured soft matrix but the martensitic transformation can be also facilitated owing to more drastic deformation incompatibility, while more sustainable TRIP effect is realized in the single-phase hetero-structures.

Declaration of Competing Interest

The authors declare that they have no known competing financial interests or personal relationships that could have appeared to influence the work reported in this paper.

Acknowledgement

The authors are grateful for the financial support of the National Key R&D Program of China (No. 2017YFB0703003), National Natural Science Foundation of China (nos. U1564203, 51571141, 51831002 and 51201105). Use of the Advanced Photon Source is supported by the U.S. Department of Energy, USA, Office of Science, Office of Basic Energy Sciences, under Contract No. DE-AC02-06CH11357.

Supplementary materials

Supplementary material associated with this article can be found, in the online version, at doi:10.1016/j.scriptamat.2020.10.041.

References

[1] M.M. Wang, C.C. Tasan, D. Ponge, A.C. Dippel, D. Raabe, Acta Mater. 85 (2015) 216–228.
[2] R. Ding, D. Tang, A. Zhao, H. Guo, J. He, C. Zhi, Mater. Des. 87 (2015) 640–649.
[3] B.B. He, B. Hu, H.W. Yen, G.J. Cheng, Z.K. Wang, H.W. Luo, M.X. Huang, Science 357 (2017) 1029.
[4] J. Liu, Y. Jin, X. Fang, C. Chen, Q. Feng, X. Liu, Y. Chen, T. Suo, F. Zhao, T. Huang, H. Wang, X. Wang, Y. Fang, Y. Wei, L. Meng, J. Lu, W. Yang, Sci. Rep. 6 (2016) 35345.
[5] M. Wendler, C. Ullrich, M. Hauser, L. Krüger, O. Volkova, A. Weiß, J. Mola, Acta Mater. 133 (2017) 346–355.
[6] Q. Han, Y. Kang, P. Hodgson, N. Stanford, Scr. Mater. 69 (2013) 13–16.
[7] G. Niu, Q. Tang, H.S. Zurob, H. Wu, L. Xu, N. Gong, Mater. Sci. Eng. A-Struct. Mater. Prop. Microstruct. Process. 759 (2019) 1–10.
[8] X. Wu, P. Jiang, L. Chen, F. Yuan, Y.T. Zhu, Proc. Natl. Acad. Sci. 111 (2014) 7197.
[9] Y.M. Wang, T. Voisin, J.T. McKeown, J. Ye, N.P. Calta, Z. Li, Z. Zeng, Y. Zhang, W. Chen, T.T. Roehling, R.T. Ott, M.K. Santala, Philip J. Depond, M.J. Matthews, A.V. Hamza, T. Zhu, Nat. Mater. 17 (2017) 63–71.
[10] J. Su, D. Raabe, Z. Li, Acta Mater. 163 (2019) 40–54.
[11] Y. Zhu, X. Wu, Mater. Res. Lett. 7 (2019) 393–398.
[12] J. Li, Q. Zhang, R. Huang, X. Li, H. Gao, Scr. Mater. 186 (2020) 304–311.
[13] L.G. Sun, G. Wu, Q. Wang, J. Lu, Mater. Today (2020).
[14] Y. Li, W. Li, N. Min, W. Liu, C. Zhang, X. Jin, Scr. Mater. 178 (2020) 211–217.
[15] R. Saha, R. Ueji, N. Tsuji, Scr. Mater. 68 (2013) 813–816.
[16] C.X. Huang, W.P. Hu, Q.Y. Wang, C. Wang, G. Yang, Y.T. Zhu, Mater. Res. Lett. 3 (2014) 88–94.
[17] C. Lei, X. Deng, X. Li, Z. Wang, Scr. Mater. 162 (2019) 421–425.
[18] J.H. Hwang, T.T.T. Trang, O. Lee, G. Park, A. Zargaran, N.J. Kim, Acta Mater. 191 (2020) 1–12.
[19] V.S.A. Challa, X.L. Wan, M.C. Somani, L.P. Karjalainen, R.D.K. Misra, Mater. Sci. Eng. A 613 (2014) 60–70.
[20] B. Sun, Y. Ma, N. Vanderesse, R.S. Varanasi, W. Song, P. Bocher, D. Ponge, D. Raabe, Acta Mater. 178 (2019) 10–25.
[21] B. Fu, W.Y. Yang, Y.D. Wang, L.F. Li, Z.Q. Sun, Y. Ren, Acta Mater. 76 (2014) 342–354.
[22] M.N. Hasan, Y.F. Liu, X.H. An, J. Gu, M. Song, Y. Cao, Y.S. Li, Y.T. Zhu, X.Z. Liao, Int. J. Plast. 123 (2019) 178–195.
[23] R. Song, D. Ponge, D. Raabe, Acta Mater. 53 (2005) 4881–4892.
[24] Y. Zhao, T. Yang, Y. Tong, J. Wang, J. Luan, Z. Jiao, D. Chen, Y. Yang, A. Hu, C. Liu, Acta Mater. 138 (2017) 72–82.
[25] Y. Wei, Y.Q. Li, L. Zhu, Y. Liu, X. Lei, G. Wang, Y. Wu, Z. Mi, J. Liu, H. Wang, Nat. Commun. 5 (2014) 3580 -3580.
[26] X. Peng, D. Zhu, Z. Hu, W. Yi, H. Liu, M. Wang, Mater. Des. 45 (2013) 518–523.
[27] A. Eres-Castellanos, F.G. Caballero, C. Garcia-Mateo, Acta Mater. 189 (2020) 60–72.
[28] P. Sathiyamoorthi, H.S. Kim, Prog. Mater. Sci. (2020) 100709.